

AUTOMATED INSPECTION OF CONTOUR FAULTS FOR CONVEX MIRRORS USING WAVELET DESCRIPTORS AND EWMA CONTROL SCHEME

HONG-DAR LIN* AND YU-KAI LIN

Department of Industrial Engineering and Management
Chaoyang University of Technology
No. 168, Jifong East Road, Wufong District, Taichung 41349, Taiwan
*Corresponding author: hmlin@cyut.edu.tw

Received March 2020; revised June 2020

ABSTRACT. *Side and rear car mirrors are among the most important safety features on our vehicles. Ordinary appearance faults of car mirrors comprise surface fault type and contour fault type. Since the contour faults will cause structural damages on vehicle mirrors and reduce the ability to withstand outer stress and pressure, the degree of harm is even more than the surface faults for vehicle mirrors. To substitute examiners from traditional inspection tasks of car mirrors, this study exploits a hybrid method based on computer vision to inspect contour faults on convex car mirrors. The hybrid method consists of wavelet transform and small variation detection algorithm. Distances from boundary points of a mirror to the centroid are transformed to 1-D wavelet domain with low-pass filtering to enhance the contour faults on the binary mirror images. The distance deviations of the corresponding boundary points before and after applying the wavelet filtering process can be distinguished by the exponential weighted moving average model to identify locations of the contour faults. This approach only uses self-own information of testing images to determine whether there are any irregular contour changes without the need of standard patterns for matching. Experimental outcomes show that the proposed hybrid method reaches 7% incorrect alert rate and 86% fault detection rate for the front-view image inspection; 5% incorrect alert rate and 92% fault detection rate for the side-view image inspection and it outperforms the existing methods in contour faults inspection on convex car mirrors.*

Keywords: Automated industrial inspection, Convex car mirrors, Contour faults, Wavelet descriptors, EWMA model

1. Introduction. Vehicle mirrors allow light to be reflected so that the objects behind the car can be seen. Curved convex vehicle mirrors can make driver's rear view more widely. The side and rear vehicle mirrors are among the most important safety features on our vehicles. Since appearance faults straight influence product quality of mirrors, the inspection of appearance faults is very important for producers. In the production process of mirror related products, a metal is coated on the rear of see-through glass to make better the effect of reflection. Laboring examination is simple to be disturbed by the outer object images reflected on the appearances of mirrors and leads to making wrong decisions in the defect inspection. Moreover, the exterior of a mirror product is simply fastened to dust, dirt, water, and so on and makes the flaw inspection work more difficult. Figure 1 shows a regular side car mirror and a work-in-process (WIP) car mirror.

General appearance faults of vehicle mirrors include primarily: scratches, bubbles, pin-holes, belonging to the surface fault type; and damaged edges, burrs, belonging to the



FIGURE 1. (a) A side car mirror; (b) a WIP car mirror

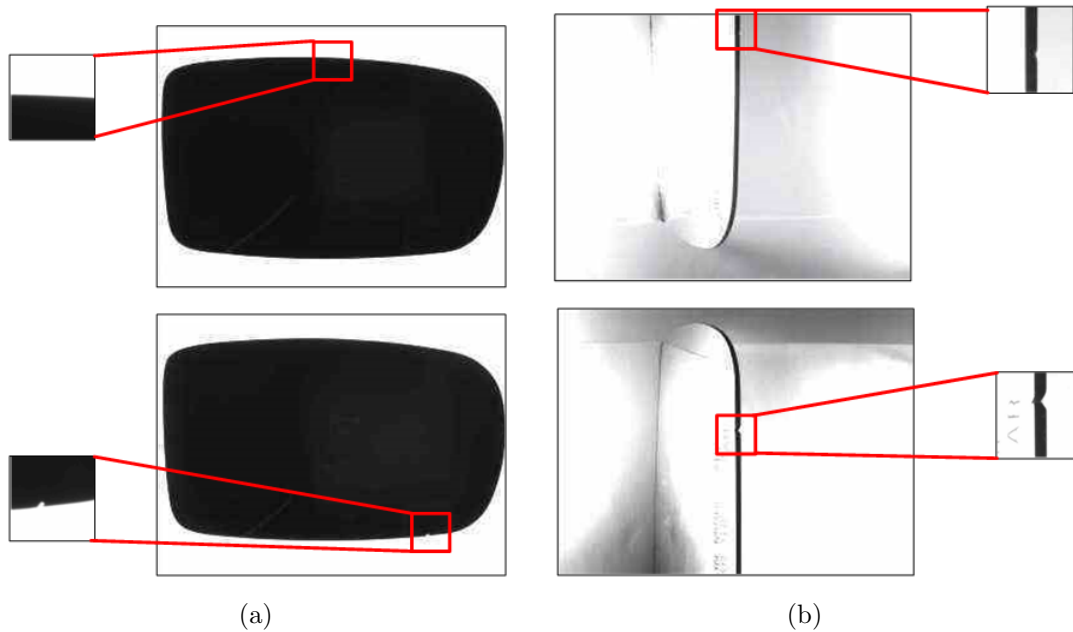


FIGURE 2. Corresponding contour faults appearing on car mirrors: (a) from front-view images; (b) from side-view images

contour fault type. Since the contour faults will cause structural damages on vehicle mirrors and reduce the ability to withstand outer stress and pressure, the degree of harm is even more than the surface faults for vehicle mirrors. After performing the grinding operation, the burr faults almost do not exist. The damages edges are the main flaws in the contour fault type. The defect sizes of common car mirrors needed to be inspected out are at least 0.20 mm for the surface fault type and 0.26 mm for the contour fault type. Appearance faults on the curved convex surfaces are hard to be examined for technical inspectors because of light reflection on mirror surfaces. In this study, we investigate the trial WIP car mirrors with length 18.1 cm, width 10.71 cm, and thickness 0.2 cm, arbitrarily chosen from the production lines of car mirrors. To clearly identify the contour faults on car mirrors, ideal visual examinations from one front view, one back view, and four side views will be conducted on mirror samples.

A car mirror has a rectangular form with round corners and curve surface and the contour faults to be inspected can be found on the outer edges of the mirror. The curved mirror has the surface of higher reflection and wider field of view which is more complex than that of the plane mirror of vehicle. The majority of contour faults are highly of many kinds and can suppose different forms. Figure 2 shows the locations of contour

faults on car mirrors displayed on both front-view images and corresponding side-view images. Some contour faults do not appear simultaneously on both of the front-view image and side-view image due to various locations, shapes, sizes of faults. Therefore, the two types of images need to be investigated to make sure the existence of contour faults.

Since car mirrors have high reflective surfaces, those reflected lightings make the flaw inspection work more difficult when contour faults are inlaid on the curved surfaces of car mirrors. High reflection on curved mirrors grows the difficulty of distinguishing the contour faults on car mirrors. The angle diversity of capturing images makes it more difficult to implement an automated fault inspection. Therefore, this study establishes an automated contour fault inspection system of car mirrors to replace manual inspectors from car mirror inspection tasks. We propose a wavelet descriptors based small variation detection technique to examine contour faults on curved car mirrors.

The rest of the article is composed as follows. Firstly, we review the articles on current techniques of image processing for appearance flaw inspection. Secondly, we describe the proposed image procedures for detecting contour faults on car mirrors. Thirdly, we execute the trials and assess the manifestation of the suggested model with traditional techniques. Finally, we conclude the contributions and indicate the further directions.

2. Literature Review. Automated optical inspection (AOI) of appearance flaws has changed into a crucial task for producers striving to upgrade goods quality and manufacturing efficiency [1,2]. AOI systems are arising in technologies that are beneficial in many manufacturing industries, such as inspection of little appearance variations on capacitor chips of passive components [3], detection of appearance defects on textured and non-textured surface parts [4], inspection of light-emitting diode (LED) chips [5]. These applications can all decrease laborious manual inspection and increase product quality as well as productivity by reducing both inspection time and human mistakes [6].

Illumination and reflectance are two key components in machine vision applications. If the illumination source and the characteristics of the imaged objects are not matched well, then the machine vision system may not deliver the reliable data required. Numerous research examined the appearance defect detection of glass-related goods with refractive and reflective surfaces, such as inspection of linear defects [7] and area blemishes [8] on surfaces of capacitive touch displays, inspection of surface defects on the mobile phone cover glass [9], detection of appearance defects on clear LED lenses [10] and textured LED lenses [11]. These vision systems proposed suitable lighting devices and configurations for image acquisitions and effective algorithms for defect identifications on various glass-related goods.

Some studies further focused on investigating the appearance fault inspection of mirror products with higher reflective surfaces. Chang et al. [12] developed an optical inspection platform for surface defect detection on both of flat mirrors and touch panel glass. For the car mirror inspections, Chiu et al. [13] addressed a Hough transform method for visual distortion blemish inspection on transparent glass of car mirrors. Also, Lin and Hsieh [14] developed an optical inspection system with small-shift detection skills to find reflection distortion on curved car mirrors. From the above literature reviews, almost all of the present studies regarding the glass-related products concentrate on industrial inspections of optical lenses, transparent glass, and mirrors. These optical inspection systems focus mainly on the surface and distortion defect detections. Since the contour faults could cause structural damages of products and reduce ability to withstand stress, the degree of harm is even more than the surface and distortion defects. Accordingly, we apply wavelet descriptors and variation detection method to contour fault inspection on curved car mirrors with high reflective surfaces.

A remarkable shape characteristic of an object in a binary image is its object contour. Shape information is conveyed through changes in the slopes of an object's boundary. The greatest change of the slopes is also called the largest curvature. Corner detection is identical to find the high curvature points on planar curve. Many corner detection methods calculated curvature maxima points using k-cosines as corners [15]. They are applied to damage detection in civil engineering [16,17] and defect detection in manufacturing industry [18]. The curvature-based methods generally suffer from shortage of rotation, translation, and scaling invariance, sensitivity to object deformations, and need referential images for template matching [16,17].

Fourier descriptors are one of the highly employed shape expression schemes. The Fourier descriptors utilize the Fourier transformed borders as the shape features. Related studies used the Fourier transform based shape descriptors and its derivatives in object analysis, such as fruit quality grading of mangoes [19], fast detection of surface defects on micro-optical elements [20], object recognition in remote sensing images [21]. The Fourier descriptors are simple to normalize data and are invariant to shape's rotation, scaling, translation, and changes of different starting points of boundary [22,23].

Wavelet transform permits a spatial-frequency decomposition of the input signal and level of frequency resolution in wavelet domain is classically contemplated very coarse for experiential spatial-frequency analysis [24,25]. The wavelet transform can be utilized to depict a specified object form by wavelet descriptors. They were applied to identifying objects on the basis of their profile form by originating in a number of wavelet descriptors and contrasting them with those of specified profile patterns [26]. Some studies proposed mixed methods based on wavelet transform for defect detections, such as combining with Hilbert transform to extract fault signal for detection of rolling bearing defects [27] and prediction of gear tooth defects [28], fusing with empirical mode analysis to detect induction motor defects [29]. The wavelet functions have excellent localization capabilities in both spatial and frequency domains, allowing well expression of the local properties of the patterns. Thus, the wavelet descriptors outperform the Fourier descriptors because they have abilities to capture smaller differentiation between patterns [30].

Wavelet transform has the advantages of being fine enough to extract necessary information from the decomposed components and representing the multi-resolution decomposition. The variation detection method, exponentially weighted moving average (EWMA), is frequently applied in statistical quality control to investigating the small change or deviation from regular production processes [31-33]. Such advantages of wavelet transform combining with small variation detection method make the proposed approach suitable and favorable for our study of contour fault detection on car mirrors.

3. Proposed WEWMA Approach. This study proposes a wavelet transformation based exponentially weighted moving average (WEWMA) approach to inspect contour faults for convex car mirrors. Two types of images called front-view images and side-view images are captured from two views of real car mirror samples as the testing images. Five steps are developed to accomplish the procedure of contour fault inspection. Firstly, image preprocessing is carried out to eliminate background region and produce a binary edge image of the input image by applying the Otsu method [34] for object segmentation and Sobel edge detector [15] for edge detection to obtain the edge information of the object. Secondly, the distances from mirror boundary points to object centroid are calculated for describing the object shape and then are transformed to wavelet domain. Thirdly, by selecting a proper decomposition level in frequency domain, the low-frequency components are retained and the others are assigned to zero for rebuilding the object shape. Fourthly, the filtered frequency components are conducted by the reverse 1-D wavelet transform to

produce rebuilt distances. Then, distance deviations can be computed from comparing the original and rebuilt distances of the object boundary points. Fifthly, the EWMA model is applied to the distance deviations for detecting contour faults. Therefore, the contour faults on the curved convex car mirrors can be exactly identified and located by the proposed approach. Figure 3 describes the flow chart of the suggested method.

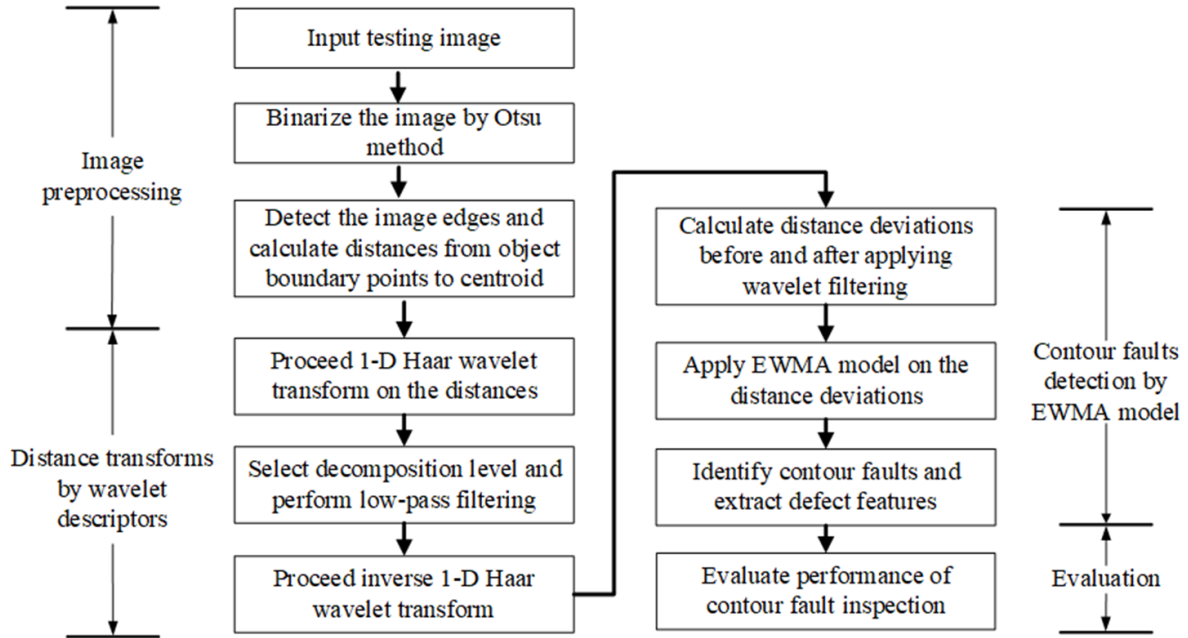


FIGURE 3. Flow chart of the proposed WEWMA approach

3.1. Image preprocessing procedure. For obtaining better image quality and inspection performance, a testing sample is divided into 7 parts for image acquisition. An entire testing sample is captured into one front-view image and six side-view images to clearly display the details of mirror contours on each image (Figure 4). This study uses the Otsu method to binarize the testing images for segmenting mirrors from backgrounds and then applies the Sobel edge detector to the binary images for obtaining boundary information of the mirrors. Figure 5 shows the results in the process of image binarization and edge detection, the binary images and edge images. The boundary information of objects in each image is clearly recorded. Then, we calculate the distances from mirror boundary points to object centroid in each image for further data transformation.

We assume a mirror with k boundary points and a centroid C . The Euclidean distance vector \mathbf{D} between the k boundary points (x_i, y_i) and the centroid $C(x_c, y_c)$ is calculated as

$$\mathbf{D} = \{d_1, d_2, \dots, d_k\}, \quad d_i = \sqrt{(x_i - x_c)^2 + (y_i - y_c)^2}, \quad (1)$$

$$C = (x_c, y_c), \quad x_c = \frac{\sum_{i=1}^k x_i}{k}, \quad y_c = \frac{\sum_{i=1}^k y_i}{k}$$

We normalize the Euclidean distance vector \mathbf{D} to obtain the scaling-invariant vector \mathbf{U} ,

$$\mathbf{U} = (u_1, u_2, \dots, u_i, \dots, u_k), \quad u_i = \frac{d_i}{\max(\mathbf{D})}, \quad i = 1, 2, \dots, k \quad (2)$$

The normalized distance vector describing the shape of an object will be utilized as the input for 1-D wavelet transformation.

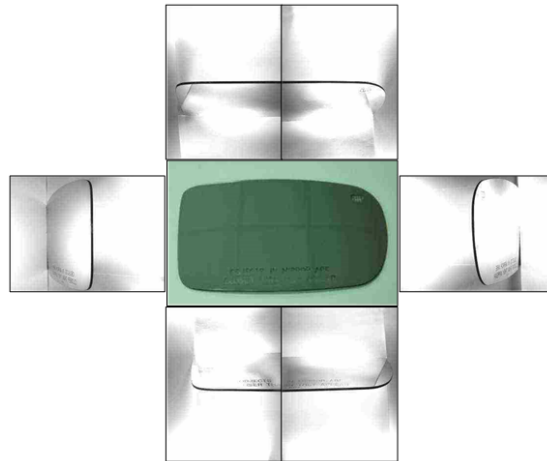


FIGURE 4. One front-view image and six side-view images captured from a mirror sample

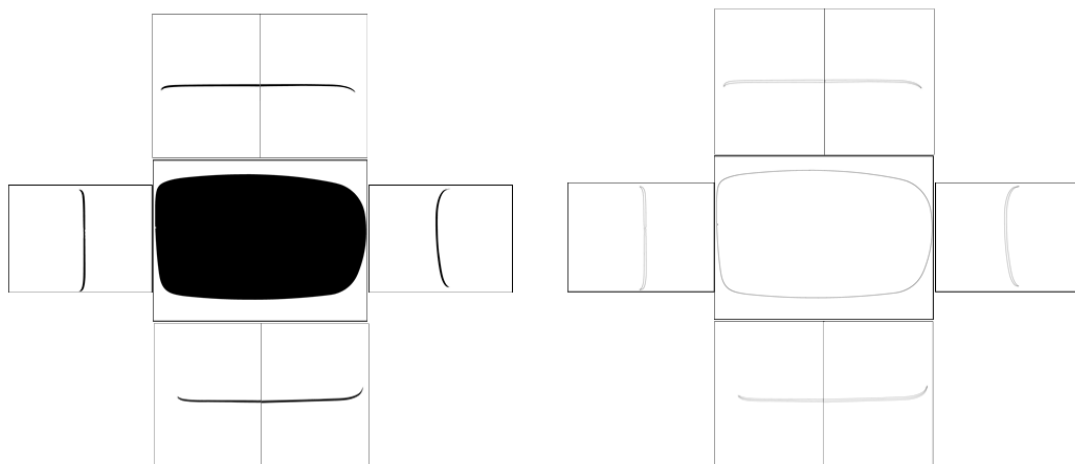


FIGURE 5. The binary images and edge images after applying the Otsu method and Sobel edge detector in the testing images

Figure 6 shows the edge images and corresponding distance diagrams of the boundary points to centroids of objects. Figures 6(a1) and 6(b1) are the edge images with marked corners and contour faults for the front-view image and side-view image, respectively. Figures 6(a2) and 6(b2) are the corresponding distance diagrams of boundary points to centroids of objects for the front-view image and side-view image. The corner points with notable and gradual changes on curves can be significantly identified in the distance diagrams. However, the contour faults with little and abrupt changes on curves are hard to be detected from the distance diagrams. We need to use more reactive features and tools to identify the contour faults from the boundary points.

3.2. Wavelet filtering operation. The inspection work of this study includes detecting irregular but vague flawed items, visual faults on the contours of highly reflective car mirrors. Lots of these unforeseen faults are exceedingly little in size and cannot be quantized by clear measures, thereby making automatic fault inspection difficult. With excellent spatial-frequency distinction ability and adjustable windows, the wavelet transform is more efficient in expressing and discovering local characteristics of a curve because of the time and frequency localization features of wavelet functions [35]. We employ the Haar

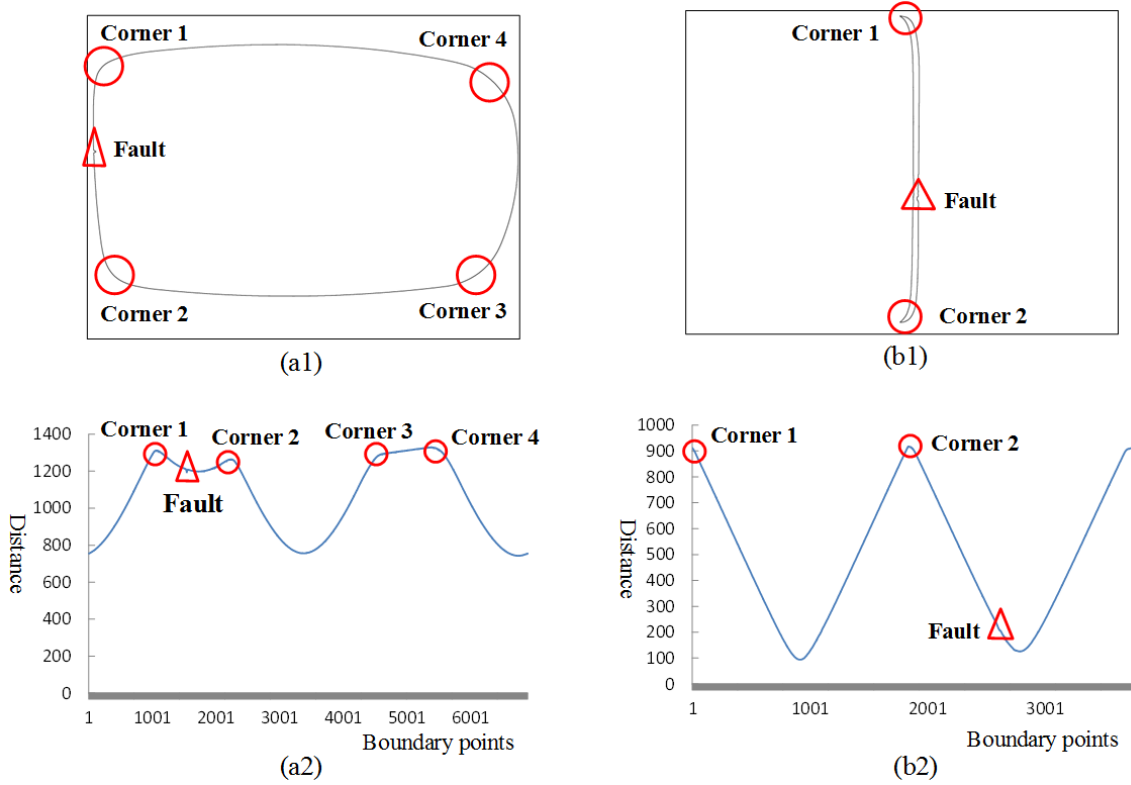


FIGURE 6. The edge images and corresponding distance diagrams of boundary points to centroids of objects: (a) for the front-view image; (b) for the side-view image

wavelet transform to execute image transformation for frequency filtering because the merits of Haar function include easy implementations, fast processing, memory saving, and many signal characteristics [24].

For one layer of Haar wavelet decomposition on the normalized distance vector \mathbf{U} , we obtain a vector of low-frequency components \mathbf{L}^1 and a vector of high-frequency components \mathbf{H}^1 . This one layer of wavelet decomposition is denoted as follows,

$$\begin{aligned} \mathbf{U} &\xrightarrow{Haar^1} (\mathbf{L}^1 | \mathbf{H}^1), \quad \mathbf{L}^1 = (L_1^1, L_2^1, \dots, L_i^1, \dots, L_{k/2}^1), \\ \mathbf{H}^1 &= (H_1^1, H_2^1, \dots, H_i^1, \dots, H_{k/2}^1) \end{aligned} \tag{3}$$

where $L_1^1 = (u_1 + u_2)/\sqrt{2}$, $L_2^1 = (u_3 + u_4)/\sqrt{2}$, ..., $L_i^1 = (u_{2i-1} + u_{2i})/\sqrt{2}$, and $H_1^1 = (u_1 - u_2)/\sqrt{2}$, $H_2^1 = (u_3 - u_4)/\sqrt{2}$, ..., $H_i^1 = (u_{2i-1} - u_{2i})/\sqrt{2}$.

The Haar transform can be calculated stepwise by the mean value and half of the difference of two adjacent normalized distance values and then multiplying the average and half the difference by $\sqrt{2}$. The multiplication by $\sqrt{2}$ is needed in order to ensure that the Haar transform preserves the energy of a signal [36]. The second layer of wavelet decomposition is further decomposing the low-frequency components \mathbf{L}^1 and denoted as follows,

$$\begin{aligned} \mathbf{L}^1 &\xrightarrow{Haar^2} (\mathbf{L}^2 | \mathbf{H}^2), \quad \mathbf{L}^2 = (L_1^2, L_2^2, \dots, L_i^2, \dots, L_{(k/2)/2}^2), \\ \mathbf{H}^2 &= (H_1^2, H_2^2, \dots, H_i^2, \dots, H_{(k/2)/2}^2) \end{aligned} \tag{4}$$

where $L_1^2 = (L_1^1 + L_2^1)/\sqrt{2}$, $L_2^2 = (L_3^1 + L_4^1)/\sqrt{2}$, ..., $L_i^2 = (L_{2i-1}^1 + L_{2i}^1)/\sqrt{2}$, and $H_1^2 = (L_1^1 - L_2^1)/\sqrt{2}$, $H_2^2 = (L_3^1 - L_4^1)/\sqrt{2}$, ..., $H_i^2 = (L_{2i-1}^1 - L_{2i}^1)/\sqrt{2}$.

By selecting a proper decomposition level in frequency domain, the low-pass filtering means the low-frequency components are retained and the others are assigned to zero (e.g., $\mathbf{H}^2 = 0$ for second layer decomposition) for rebuilding the object shape. Assume the low-frequency components in the first layer decomposition be $\mathbf{l}^1 = (l_1^1, l_2^1, \dots, l_i^1, \dots, l_{k/2}^1)$, the inverse wavelet transform of the low-pass filtering in the second layer decomposition can be denoted as

$$\mathbf{l}^1 \stackrel{H_{aar2}}{\leftarrow} (\mathbf{L}^2 | \mathbf{H}^2), \quad \mathbf{L}^2 = (L_1^2, L_2^2, \dots, L_i^2, \dots, L_{(k/2)/2}^2), \quad \mathbf{H}^2 = (0, 0, \dots, 0) \quad (5)$$

where $l_1^1 = \frac{\sqrt{2}(L_1^2+0)}{2}$, $l_3^1 = \frac{\sqrt{2}(L_2^2+0)}{2}$, \dots , $l_{2i-1}^1 = \frac{\sqrt{2}(L_i^2+0)}{2}$, and $l_2^1 = \frac{\sqrt{2}(L_1^2-0)}{2}$, $l_4^1 = \frac{\sqrt{2}(L_2^2-0)}{2}$, \dots , $l_{2i}^1 = \frac{\sqrt{2}(L_i^2-0)}{2}$.

Similarly, assuming the rebuilt array be $\mathbf{W} = (w_1, w_2, \dots, w_i, \dots, w_k)$, the inverse transform of the low-pass filtering in the first layer decomposition is expressed as

$$\mathbf{W} \stackrel{H_{aar1}}{\leftarrow} (\mathbf{l}^1 | \mathbf{H}^1), \quad \mathbf{l}^1 = (l_1^1, l_2^1, \dots, l_i^1, \dots, l_{k/2}^1), \quad \mathbf{H}^1 = (0, 0, \dots, 0) \quad (6)$$

where $w_1 = \frac{\sqrt{2}(l_1+0)}{2}$, $w_3 = \frac{\sqrt{2}(l_2+0)}{2}$, \dots , $w_{2i-1} = \frac{\sqrt{2}(l_i+0)}{2}$, and $w_2 = \frac{\sqrt{2}(l_1-0)}{2}$, $w_4 = \frac{\sqrt{2}(l_2-0)}{2}$, \dots , $w_{2i} = \frac{\sqrt{2}(l_i-0)}{2}$.

Through filtering the high-frequency components in distinct decomposed layers for inverse wavelet transform, the rebuilt array will retain approximated shapes of objects and enhance exclusively general contours. There is essential information in the retained low-frequency components than that in the high-frequency components.

Figure 7 shows testing images and corresponding distance diagrams from boundary points to centroids in wavelet domain before and after applying the low-pass wavelet filtering for faultless and fault mirrors. After proceeding the low-pass wavelet filtering, not only the four corners but also the contour faults are significantly enhanced in the wavelet domain. The filtered frequency components are conducted by the inverse 1-D wavelet transform to produce rebuilt distances. Then, distance deviations can be computed from

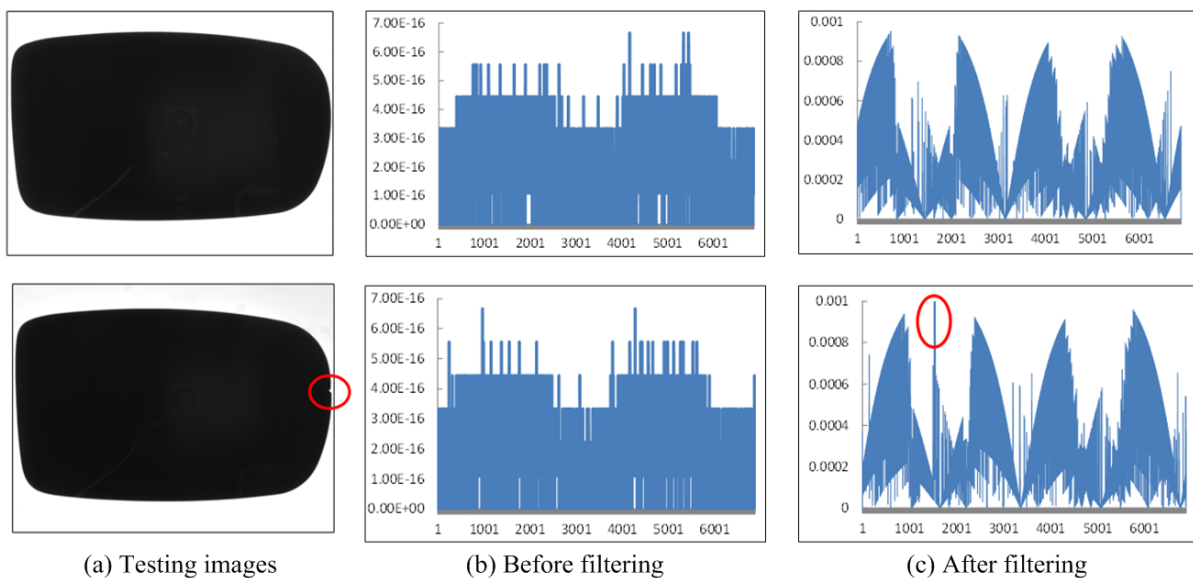


FIGURE 7. Testing images and corresponding distance diagrams from boundary points to centroids in wavelet domain before and after applying the low-pass wavelet filtering for faultless and fault mirrors

comparing the original and rebuilt distances of the object. Subsequently, the EWMA model is applied to the distance deviations for detecting contour faults.

3.3. One-sided EWMA model based on distance deviations. We assume the rebuilt distance vector be \mathbf{W} after the distance vector \mathbf{U} is conducted the wavelet low-pass filtering. The distance deviation vector \mathbf{Q} can be calculated from differences between the original and rebuilt distances of the object.

$$\mathbf{Q} = \{q_1, q_2, \dots, q_i, \dots, q_k\}, \quad q_i = |w_i - u_i| \tag{7}$$

Figure 8 shows the distance deviation diagrams for the front-view and the side-view images after applying the wavelet low-pass filtering.

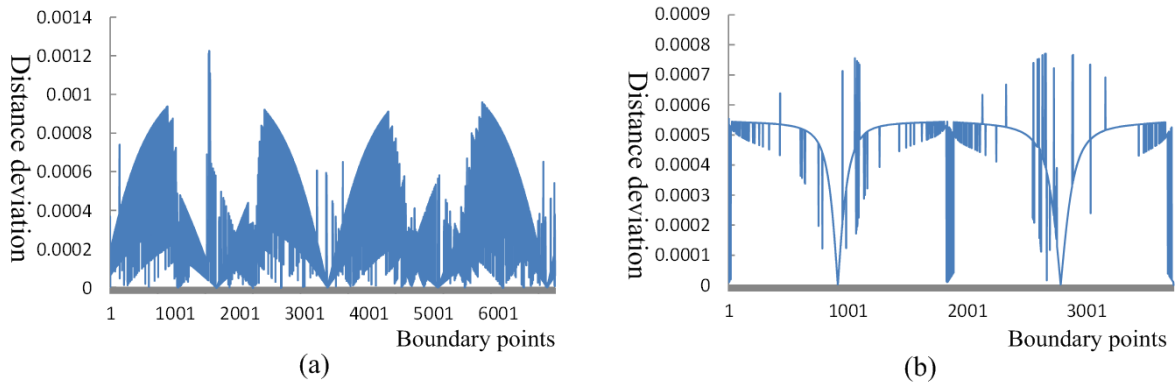


FIGURE 8. Distance deviation diagrams for (a) the front-view image and (b) the side-view image after applying wavelet low-pass filtering

There are many boundary points for a front-view image or a side view image of a mirror. For the consideration of computation efficiency, we take sampling on the data of distance deviation vector \mathbf{Q} to obtain a sampling distance deviation vector \mathbf{S} ,

$$\mathbf{S} = \{s_1, s_2, \dots, s_i, \dots, s_{k/10}\} \tag{8}$$

$s_1 = \max(q_1, q_2, \dots, q_{10})$, $s_2 = \max(q_{11}, q_{12}, \dots, q_{20})$, $s_i = \max(q_{(i-1) \times 10 + 1}, q_{(i-1) \times 10 + 2}, \dots, q_{i \times 10})$.

We select the maximum value of every 10 consecutive distance deviations as the representative value in each sampling. Figure 9 shows the sampling distance deviation diagrams of the front-view image and the side-view image. Subsequently, the EWMA model will

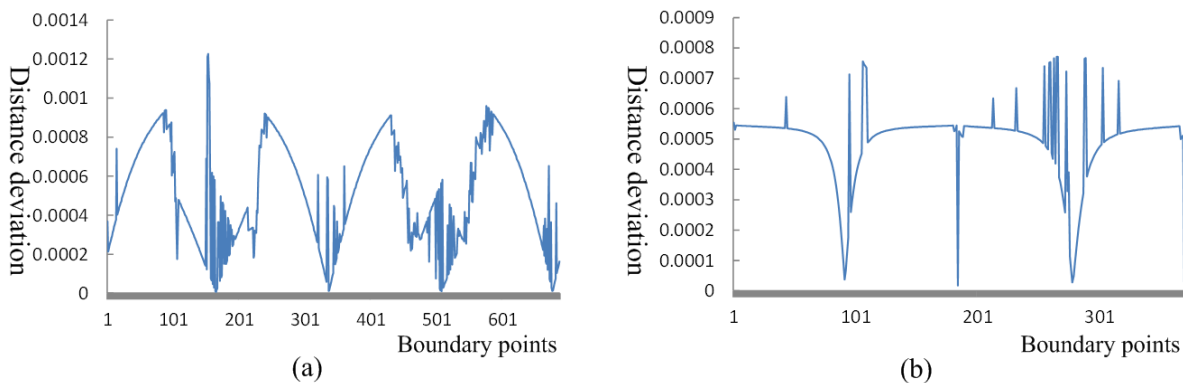


FIGURE 9. Sampling distance deviation diagrams of (a) the front-view image and (b) the side-view image

be applied on the sampling distance deviations to find slight changes of the distance deviations for detecting contour faults.

To detect slight changes in the distance deviations, this research suggests the EWMA model to investigate the small change. The exponentially weighted moving average Z_i is defined as:

$$z_i = \lambda s_i + (1 - \lambda)z_{i-1} \tag{9}$$

$$z_0 = \mu = \sum_{i=1}^{k/10} s_i \tag{10}$$

where $0 < \lambda \leq 1$ is a constant and the initial value is the process target $Z_0 = \mu_0$. The values of the parameter λ smoothing constant or called weight in the interval $0.05 \sim 0.25$ work well for small shift detection in practice [31]. The upper control limit for the one-sided EWMA control method is as follows:

$$UCL_i = \bar{X} + L\sigma \sqrt{\frac{\lambda}{2 - \lambda} [1 - (1 - \lambda^{2i})]} \tag{11}$$

The parameter settings of the model are the multiple of standard deviation utilized in the upper control limit (L) and the value of λ . The manifestation of the EWMA control technique is excellent in small-change detection, and in some ways it is easier to establish and work [37]. Figure 10 shows the contour faults are correctly identified by the EWMA model in both front-view image and side-view image. The results indicate that the contour faults on car mirrors are correctly separated in the binary image, in spite of mirrors with high reflection.

In this study, we investigate a supervised contour inspection issue. Supervised systems are general in automated optical inspection and are suitable for controlled conditions

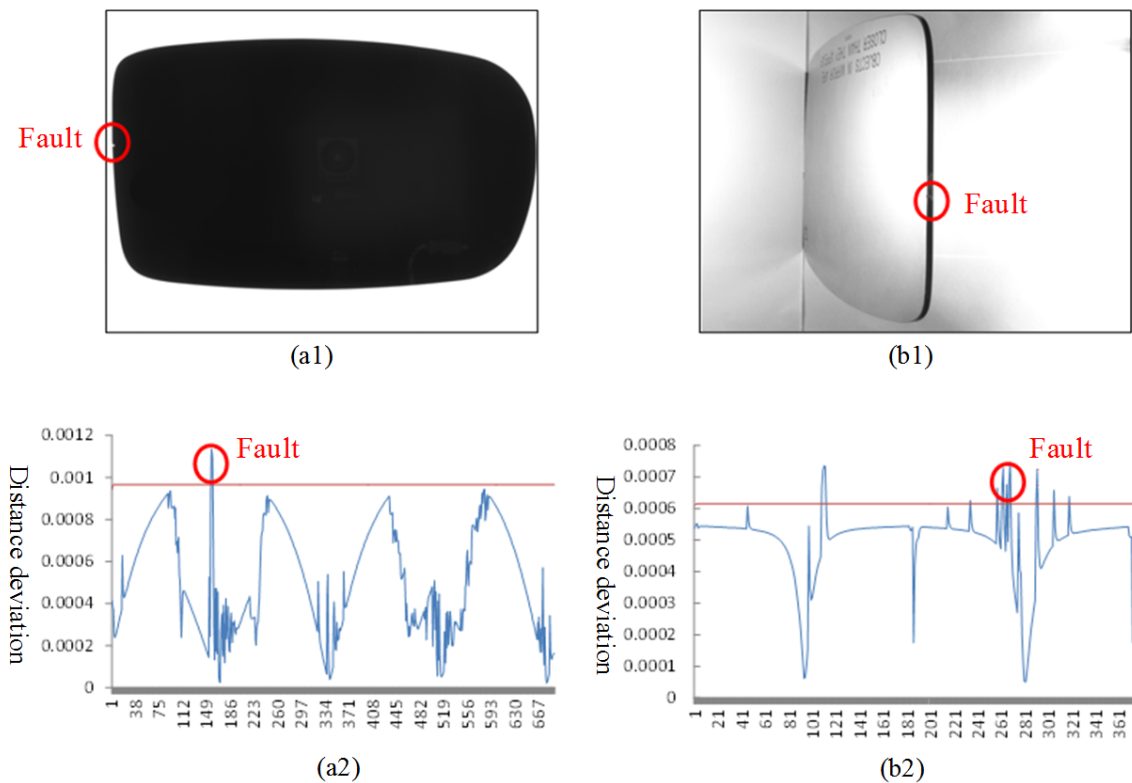


FIGURE 10. The contour faults are correctly identified by the EWMA model in both front-view image and side-view image.

in manufacturing processes. The number of decomposition levels of wavelet transform filtering and the parameter settings used for EWMA model are prearranged from a training stage. The influence of number of multi-resolution levels and EWMA parameters on inspection outcomes are empirically assessed in the next section.

4. Implementation and Analyses. In this section, we carry out the proposed approach and execute trials to assess its manifestation in inspecting contour faults of objects with different shapes. To strengthen the visibility of contour faults, we utilize the following equipment in the developed vision system: a white LED backlight plate with size of 300×300 mm, a 500M-pixels color CCD, a lens with focal length 12 mm, and a three-axis XYZ electronic controlled table. Figure 11 depicts the structures of the circumstance where we scan car mirrors to be utilized as testing images in the trials. Figure 11(a) shows the setups for capturing front-view and back-view images, and Figure 11(b) is for capturing side-view images. Figures 11(c) and 11(d) are schematic diagrams for describing the placement angle (90°) for the long sides and the angle (75°) for the short sides. Experiments are conducted on real car mirrors comprising 300 testing images (100 normal images and 200 defective images) for each of capturing from front-view angle and side-view angles. Each image of the car mirror has a size of 2560×1920 pixels. This contour fault inspection arithmetic is implemented in the 6th edition of C++ Builder compiler on a computer (Intel Core i5-4210M CPU @ 2.60GHz 2.60 GHz).

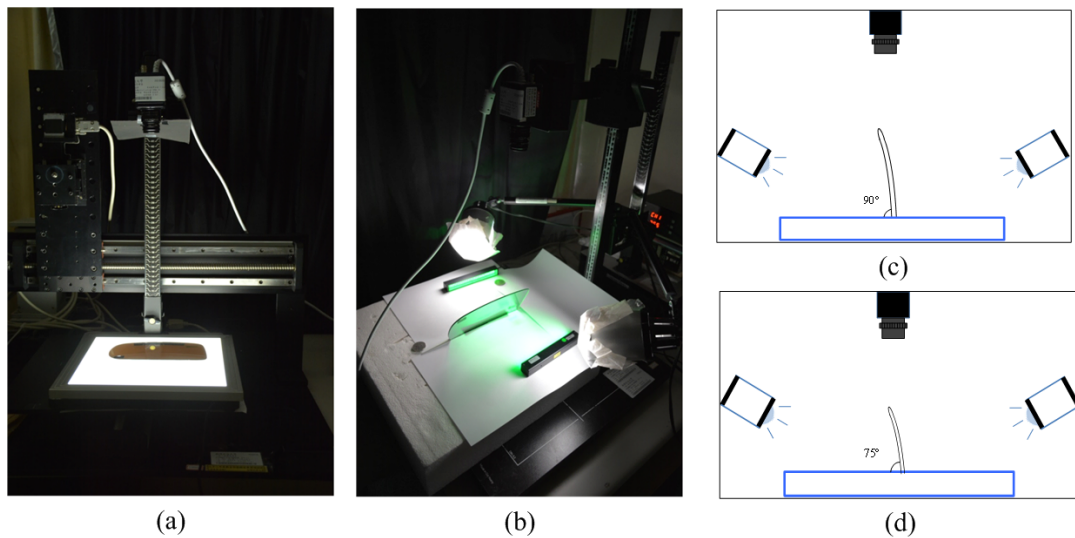


FIGURE 11. Circumstance structures of scanning a car mirror sample: (a) for capturing front-view and back-view images; (b) for capturing side-view images; (c) the placement angle for the long sides of a mirror; (d) the placement angle for the short sides

To quantitatively confirm the capability of the suggested approach, we compare the outcomes of these assessments against those provided by technical assessors (i.e., ground truth). The manifestation evaluation measures, $(1 - \alpha)$ and $(1 - \beta)$, are adopted to stand for exact inspection decisions; the larger the two measures, the more exact the inspection results [38]. Incorrect alert rate (α , regarding normal districts as contour faults), divides the area of regular districts inspected as contour faults by the area of real regular districts to obtain the mistake. Absent alert rate (β , failing to alert real contour faults), divides the area of undetected real contour faults by the area of real contour faults to obtain the mistake.

4.1. Parameter settings of the proposed method. The WEWMA method including two procedures, wavelet descriptors and EWMA model, has some parameters needed to be determined based on inspection performance. We use a small sample size with 60 defective images to conduct experiments to search for better parameter settings of the proposed approach. The distance arrays applying wavelet filtering in a suitable breakdown level will effectively enhance partial contour faults on mirror images. Figures 12 and 13 show three distance deviation diagrams after applying the low-pass wavelet filtering operations with breakdown levels 1, 2, and 3 for a front-view image and a side-view image, separately. To evaluate the influence of changing the number of breakdown levels on rebuilt results, Table 1 presents the fault detection results for the breakdown levels 1, 2, and 3. All these distance diagrams are individually rebuilt from a filtered high-frequency part and a retained low-frequency part with the Haar wavelet. The distance diagrams of the front-view image demonstrate that too little the number of breakdown level (e.g., 1) cannot adequately separate faults from the mirror contours and leads to lots of incorrect alerts. However, too big the number of breakdown levels (e.g., 2 and 3) for the side-view image produces the diverse effect of the faults and causes many missing alerts. The numbers of breakdown levels, 2 for the front-view images and 1 for the side-view images, are more appropriate to emphasize contour faults in the rebuilt distance arrays. Our trials on a variety of testing images have verified that wavelet breakdown levels 1 and 2 are ordinarily appropriate for this contour fault inspection application.

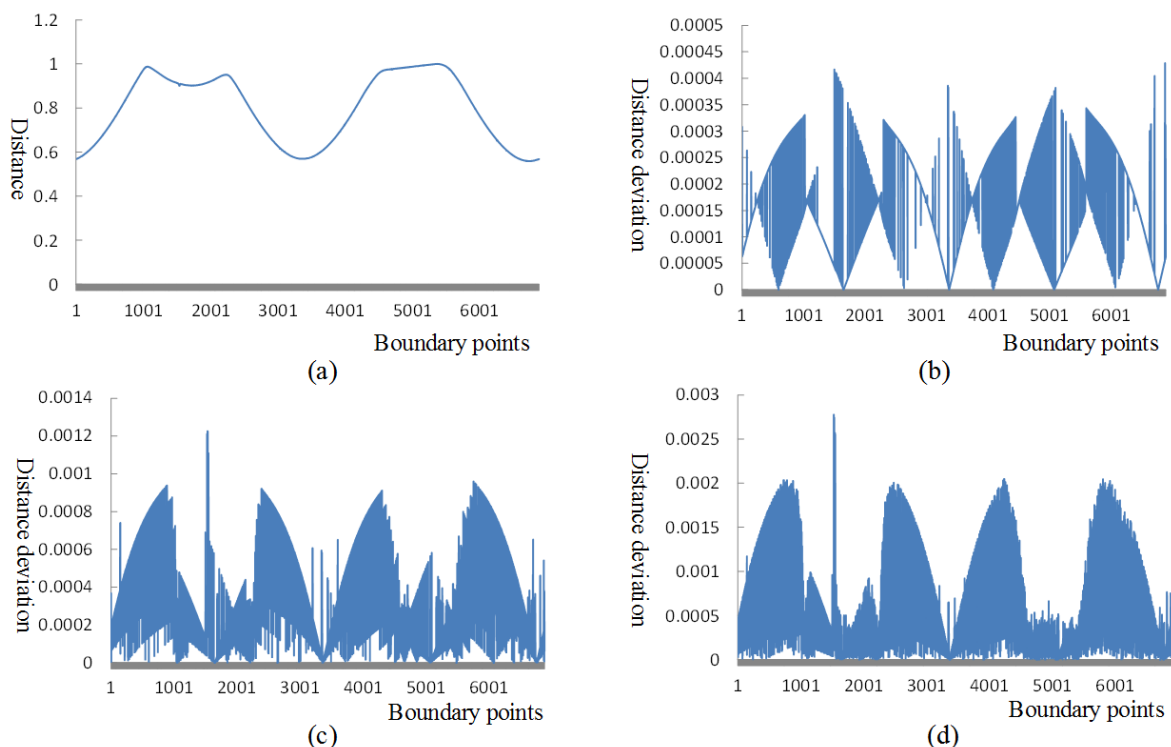


FIGURE 12. (a) A distance diagram and three distance deviation diagrams for a front-view image applying wavelet filtering operations with (b) breakdown level 1; (c) breakdown level 2; (d) breakdown level 3

Similarly, choices of the parameters λ and L determine the upper control limit of the EWMA model. The EWMA design procedure would consist of specifying the desired in-control and out-of-control average run lengths (ARL) and the magnitude of the process shift that is expected, and then to select the combination of λ and L that provide the

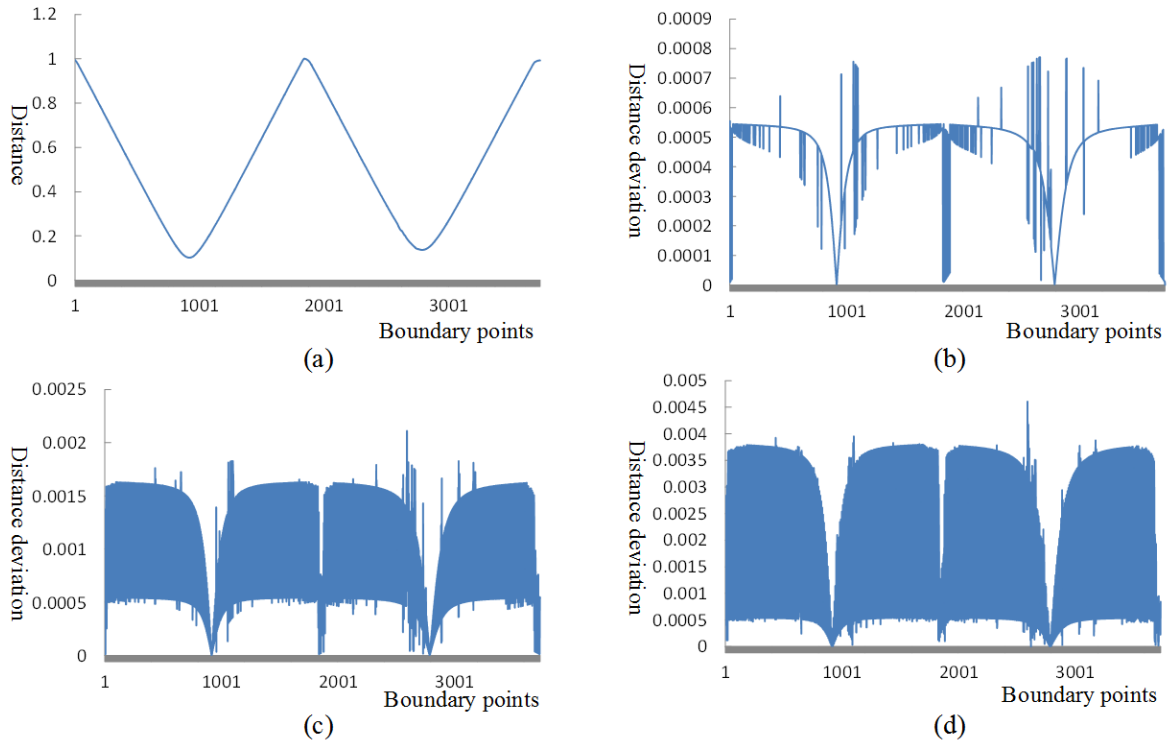


FIGURE 13. (a) A distance diagram and three distance deviation diagrams for a side-view image applying wavelet filtering operations with (b) breakdown level 1; (c) breakdown level 2; (d) breakdown level 3

TABLE 1. Performance evaluation table for front-view and side-view images inspected by the proposed method with various breakdown levels of wavelet filtering operations

Wavelet transform	Front-view images			Side-view images		
	1	2	3	1	2	3
$\alpha\%$	1.41	0.50	0.34	1.07	0.27	0.14
$(1 - \beta)\%$	80.52	80.09	60.02	83.16	52.20	24.47
CR%	98.40	99.30	99.36	98.64	98.68	98.31

desired ARL performance [31]. Although using smaller values of λ to detect smaller shifts for general two-sided EWMA charts, this study applying one-sided EWMA model uses larger values of λ to avoid the inertia effect. This effect could take the one-sided EWMA several periods to react to the shift because the small λ does not weigh the new data very heavily and reduce the effectiveness of the EWMA in shift detection [39,40].

In our experiments, Tables 2 and 3 list the performance evaluation indices based on area pixels for front-view and side-view images inspected by the proposed method with various parameter combinations (λ, L) of EWMA models, respectively. They indicate the fault detection performances of the EWMA model based on area pixels with parameter settings (λ, L) values of $(0.7, 2.2\sim 2.4)$ for front-view images and $(0.7, 1.2\sim 1.4)$ for side-view images have better detection result with erroneous alert rate less than 1.7% and fault detection rate at least 80%. For further precisely deciding both of the key parameters based on not only the area pixels but also the image numbers, we conduct more experiments to evaluate the inspection performance. Tables 4 and 5 reveal the fault detection performances of the

TABLE 2. Performance evaluation table based on area pixels for front-view images inspected by the proposed method with various parameter combinations (λ, L) of EWMA models

λ	0.5					0.6				
L	1.6	1.8	2	2.2	2.4	1.6	1.8	2	2.2	2.4
$\alpha\%$	9.37	9.92	10.36	10.77	9.86	10.45	11.31	11.62	8.58	2.66
$(1 - \beta)\%$	73.47	76.55	77.56	80.15	82.14	77.24	80.03	84.92	88.22	83.42
CR%	85.31	88.02	92.74	97.22	98.62	89.43	88.59	88.29	98.14	98.65
λ	0.7					0.8				
L	1.6	1.8	2	2.2	2.4	1.6	1.8	2	2.2	2.4
$\alpha\%$	11.98	12.18	7.92	1.70	0.44	12.70	8.19	1.67	0.48	0.37
$(1 - \beta)\%$	83.39	86.67	88.51	85.13	79.73	88.69	88.89	87.54	80.79	76.71
CR%	87.95	87.76	91.97	98.13	99.35	87.25	91.71	97.58	99.35	99.39

TABLE 3. Performance evaluation table based on area pixels for side-view images inspected by the proposed method with various parameter combinations (λ, L) of EWMA models

λ	0.5					0.6				
L	0.8	1	1.2	1.4	1.6	0.8	1	1.2	1.4	1.6
$\alpha\%$	3.75	3.01	2.02	1.55	0.85	3.64	2.59	2.04	1.05	0.73
$(1 - \beta)\%$	53.46	74.38	79.39	74.27	69.04	70.60	79.70	83.66	80.84	71.72
CR%	95.48	96.53	97.58	98.03	98.60	95.89	97.04	97.71	98.57	98.74
λ	0.7					0.8				
L	0.8	1	1.2	1.4	1.6	0.8	1	1.2	1.4	1.6
$\alpha\%$	3.50	2.50	1.52	1.02	0.75	3.07	2.17	1.44	1.04	0.69
$(1 - \beta)\%$	81.70	86.91	88.90	81.08	71.98	83.50	88.51	88.31	78.76	65.97
CR%	96.21	97.30	98.29	98.61	98.72	96.68	97.67	98.36	98.55	98.62

TABLE 4. Performance evaluation table based on area pixels and image numbers for front-view images inspected by the proposed method with various parameter combinations (λ, L) of EWMA models

λ	0.7					
L	2.2	2.25	2.3	2.33	2.35	2.4
$\alpha\%$	1.70	0.86	0.57	0.50	0.46	0.44
$(1 - \beta)\%$	85.13	83.83	82.56	80.09	79.56	79.73
CR%	98.13	98.96	99.25	99.30	99.32	99.35
Number of incorrect fault images	20/20 (100%)	13/20 (65%)	5/20 (25%)	2/20 (10%)	1/20 (5%)	1/20 (5%)
Number of correct fault images	37/40 (92.5%)	37/40 (92.5%)	37/40 (92.5%)	35/40 (87.5%)	34/40 (85%)	34/40 (85%)
Total images	60	60	60	60	60	60

EWMA model with parameter settings (λ, L) values of $(0.7, 2.33)$ for front-view images and $(0.7, 1.35)$ for side-view images have better detection results based on both criteria of area pixels and image numbers. This indicates that the more exact parameter settings of the proposed method are chosen, the better outcomes of the fault detection will have.

TABLE 5. Performance evaluation table based on area pixels and image numbers for side-view images inspected by the proposed method with various parameter combinations (λ, L) of EWMA models

λ	0.7				
L	1.2	1.25	1.3	1.35	1.4
$\alpha\%$	1.52	1.22	1.17	1.07	1.02
$(1 - \beta)\%$	88.90	87.17	85.86	83.16	81.08
CR%	98.29	98.55	98.58	98.64	98.6056
Number of incorrect fault images	5/20 (25%)	2/20 (10%)	2/20 (10%)	1/20 (5%)	1/20 (5%)
Number of correct fault images	39/40 (97.5%)	38/40 (95%)	38/40 (95%)	37/40 (92.5%)	36/40 (90%)
Total images	60	60	60	60	60

4.2. **Performance assessment of distinct detection techniques.** To assess performance of the contour fault detection on convex car mirrors with large sample size (300 testing images), two traditional schemes and the proposed method are assessed against the outcomes by professional inspectors. Figures 14 and 15 show partial results of detecting contour faults for front-view and side-view images by the curvature method, Fourier descriptors method, suggested method, and professional censor, respectively. The curvature

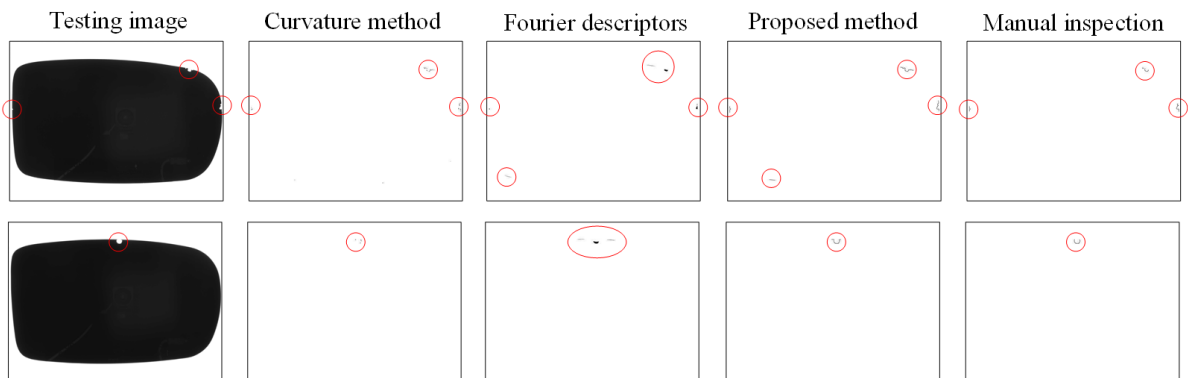


FIGURE 14. Partial detection results of the front-view images by curvature method, Fourier descriptors method, proposed method, and inspector

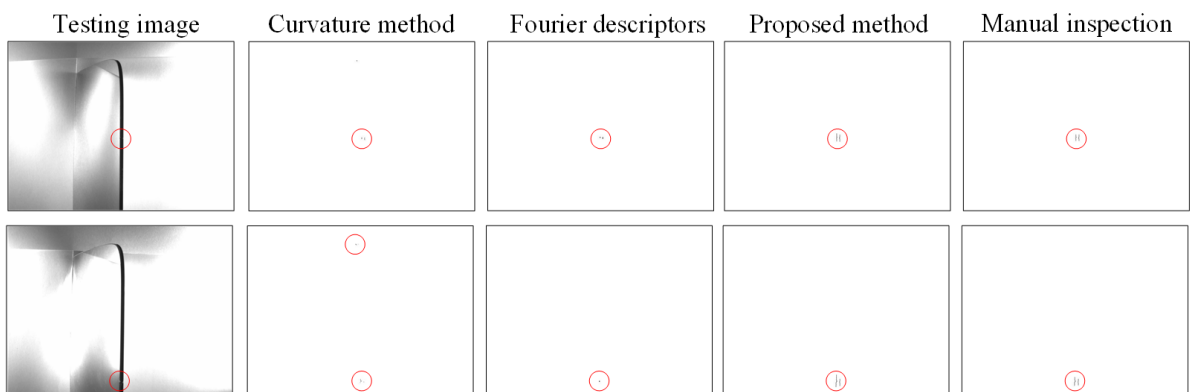


FIGURE 15. Partial detection results of the side-view images by curvature method, Fourier descriptors method, proposed method, and inspector

method makes many missing alerts in contour fault inspection. The Fourier descriptors and the suggested method inspect almost all of the contour faults and make little mistaken decisions. Thence, the frequency domain techniques surpass the spatial domain skill in the contour fault inspection of convex car mirrors.

Tables 6 and 7 sum up the inspection outcomes of our trials with large sample size. The average contour fault inspection rates ($1 - \beta$) of all testing samples based on image numbers by the three methods are, respectively, 9.0% (8.5%) by curvature method, 80% (61%) by Fourier descriptors method, and 86% (92%) by proposed method for front-view images and side-view images (shown in parentheses). Nevertheless, the two traditional methods have remarkably larger incorrect alert rates (α) based on image numbers, 15% (68%) by curvature method and 25% (23%) by Fourier descriptors method. Otherwise, the proposed approach has quite smaller incorrect alert rates, 7% (5%) for the two kinds of testing images. More concretely, the suggested method not only has larger fault inspection rates but also has smaller incorrect alert rates employed to contour fault inspection on convex mirror images.

TABLE 6. Performance evaluation table for the front-view images inspected by curvature method, Fourier descriptors method, and proposed method

	Spatial domain	Frequency domain	
	Curvature	Fourier descriptors	Proposed method
$\alpha\%$	0.07	0.013	0.34
$(1 - \beta)\%$	56.44	75.23	81.13
CR%	99.57	99.96	99.49
Number of falsely detected images	15/100 (15%)	25/100 (25%)	7/100 (7%)
Number of correctly detected images	18/200 (9%)	160/200 (80%)	172/200 (86%)
Time (Sec./image)	2.19	4.90	2.28

TABLE 7. Performance evaluation table for the side-view images inspected by curvature method, Fourier descriptors method, and proposed method

	Spatial domain	Frequency domain	
	Curvature	Fourier descriptors	Proposed method
$\alpha\%$	0.32	0.75	1.34
$(1 - \beta)\%$	31.59	62.37	84.02
CR%	98.03	98.87	98.33
Number of falsely detected images	68/100 (68%)	23/100 (23%)	5/100 (5%)
Number of correctly detected images	17/200 (8.5%)	122/200 (61%)	184/200 (92%)
Time (Sec./image)	1.85	4.84	2.21

The average processing times for inspecting an image of 2560×1920 pixels are: 1.85 seconds by curvature method, 4.84 seconds by Fourier descriptors method, 2.21 seconds by suggested method. The mean processing time of the suggested method is more than two times quicker than that of the Fourier descriptors method. The suggested method conquers the troubles of inspecting contour faults on mirror images with high reflection

and outperforms in the ability of accurately differentiating contour faults from normal regions.

4.3. Inspection of concave parts. To evaluate the performance of inspecting contour faults on concave objects as well as convex objects by the proposed approach, experiments on various concave objects are explored. Figure 16 shows the partial results of detecting contour faults on four concave objects by the proposed method. We find most of the real contour faults are detected and only very few normal districts are detected as faults on the concave objects. In applying to real industrial parts, Figure 17 shows the results of inspecting concave memory cards with faultless and contour faults by the proposed method. It indicates even very small contour faults on the concave memory cards can also be precisely identified regardless of concave or convex object shapes.

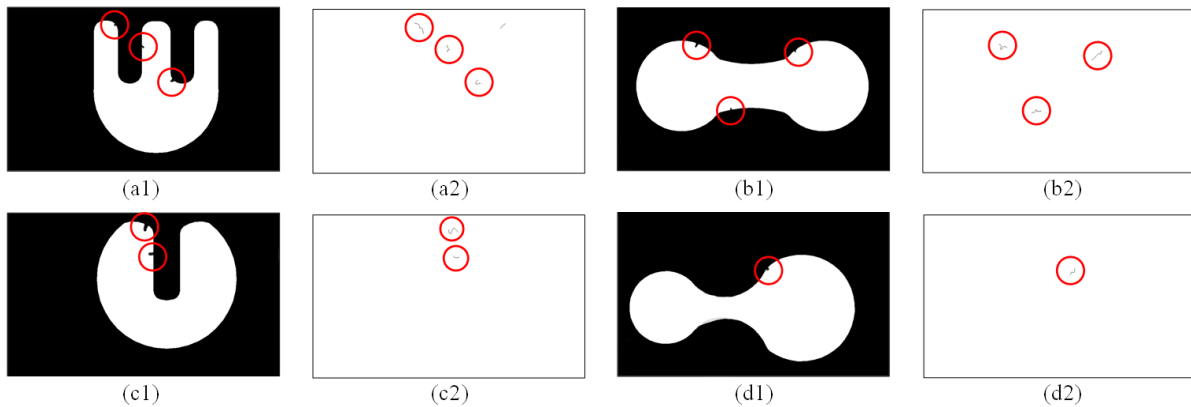


FIGURE 16. Inspection results of various concave objects with contour faults by the proposed method

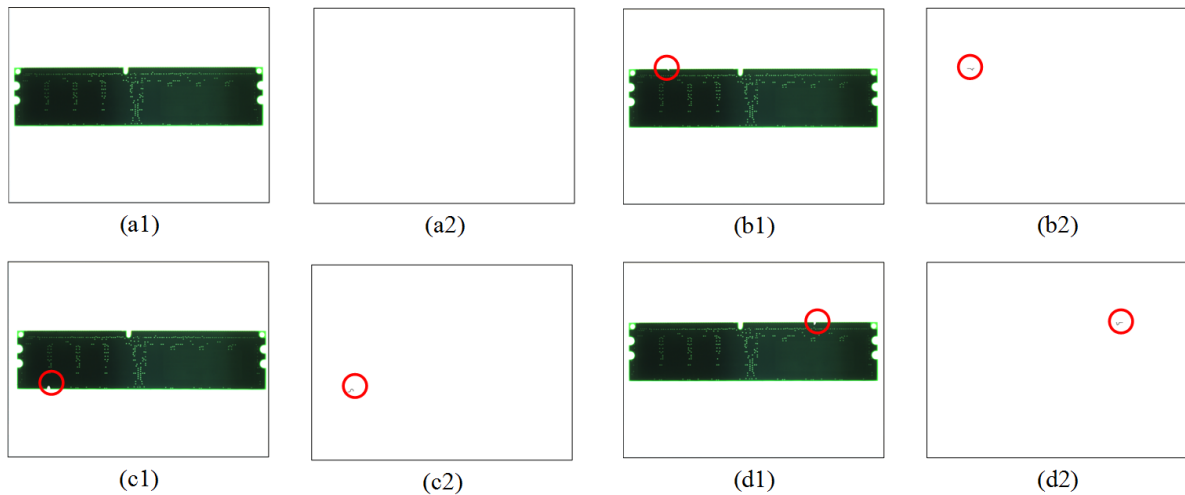


FIGURE 17. Inspection results of concave memory cards with faultless and faults by the proposed method

5. Conclusions. This research proposes a wavelet transformation based exponentially weighted moving average approach to inspect contour faults for convex car mirrors. This WEWMA scheme achieves self-comparison between the testing image and the rebuilt one and does not rely on any standard pattern for matching. This approach only uses self-own

information of the testing images to determine whether there are any irregular contour changes on object contours. Experimental results demonstrate that the proposed method reaches at least a large 81.13% probability of exactly distinguishing contour faults from rough boundaries and no more than a small 1.34% probability of incorrectly detecting normal districts as contour faults on uneven profiles of car mirrors. Major restrictions of the present method need to be conquered in the future study as follows, it will make lots of missing alerts if some contour faults are gathering in a narrow scope, and it is not reactive to discriminate the contour faults with gradual changes in shapes.

Acknowledgment. The authors thank the Ministry of Science and Technology, Taiwan, for the financial support through the Grant MOST 107-2221-E-324-016.

REFERENCES

- [1] C. J. Kuo, T. Fang and C. Lee, Automated optical inspection system for surface mount device light emitting diodes, *Journal of Intelligent Manufacturing*, vol.30, pp.641-655, 2019.
- [2] K. T. Maddala, R. H. Moss, W. V. Stoecker, J. R. Hagerty, J. G. Cole, N. K. Mishra and R. J. Stanley, Adaptable ring for vision-based measurements and shape analysis, *IEEE Trans. Instrumentation and Measurement*, vol.66, no.4, pp.746-756, 2017.
- [3] H.-D. Lin and S. W. Chiu, Automated surface micro flaw inspection for quality control of electronic chips, *International Journal of the Physical Sciences*, vol.6, no.23, pp.5528-5539, 2011.
- [4] J. K. Park, B. K. Kwon, J. H. Park and D. J. Kang, Machine learning-based imaging system for surface defect inspection, *International Journal of Precision Engineering and Manufacturing-Green Technology*, vol.3, no.3, pp.303-310, 2016.
- [5] H. Lin, B. Li, X. G. Wang, Y. F. Shu and S. L. Niu, Automated defect inspection of LED chip using deep convolutional neural network, *Journal of Intelligent Manufacturing*, vol.30, no.6, pp.2525-2534, 2019.
- [6] E. M. Taha, E. Emary and K. Moustafa, Automatic optical inspection for PCB manufacturing: A survey, *International Journal of Scientific & Engineering Research*, vol.5, no.7, pp.1095-1102, 2014.
- [7] H.-D. Lin and H. H. Tsai, Automated quality inspection of surface defects on touch panels, *Journal of the Chinese Institute of Industrial Engineers*, vol.29, no.5, pp.291-302, 2012.
- [8] Y. P. Chiu and H.-D. Lin, Creation of image models for inspecting visual flaws on capacitive touch screens, *Journal of Applied Engineering Science*, vol.16, no.3, pp.333-342, 2018.
- [9] D. Li, L. Q. Liang and W. J. Zhang, Defect inspection and extraction of the mobile phone cover glass based on the principal components analysis, *International Journal of Advanced Manufacturing Technology*, vol.73, pp.1605-1614, 2014.
- [10] H.-D. Lin and Y. S. P. Chiu, Automated flaw detection for lens components, *Advanced Science Letters*, vol.17, pp.114-121, 2012.
- [11] H.-D. Lin and H.-L. Chen, Detection of surface flaws on textured LED lenses using wavelet packet transform based partial least squares techniques, *International Journal of Innovative Computing, Information and Control*, vol.15, no.3, pp.905-921, 2019.
- [12] M. Chang, B. C. Chen, J. L. Gabayno and M. F. Chen, Development of an optical inspection platform for surface defect detection in touch panel glass, *International Journal of Optomechatronics*, vol.10, no.2, pp.63-72, 2016.
- [13] Y. P. Chiu, Y. C. Lo and H.-D. Lin, Hough transform based approach for surface distortion flaw detection on transparent glass, *International Journal of Applied Engineering Research*, vol.12, no.19, pp.8150-8159, 2017.
- [14] H.-D. Lin and K.-S. Hsieh, Detection of surface variations on curved mirrors of vehicles using slight deviation control techniques, *International Journal of Innovative Computing, Information and Control*, vol.14, no.4, pp.1407-1421, 2018.
- [15] R. C. Gonzalez and R. E. Woods, *Digital Image Processing*, 4th Edition, Pearson, New York, NY, USA, 2017.
- [16] V. B. Dawari and G. R. Vesmawala, Modal curvature and modal flexibility methods for honeycomb damage identification in reinforced concrete beams, *Procedia Engineering*, vol.51, pp.119-124, 2013.
- [17] A. Samet, Y. Hui, M. A. B. Souf, O. Bareille, M. Ichchou, T. Fakhfakh and M. Haddar, Experimental investigation of damage detection in plate-like structure using combined energetic approaches, *Proc.*

- of the Institution of Mechanical Engineers, Part C: Journal of Mechanical Engineering Science*, vol.233, no.4, pp.1193-1203, 2019.
- [18] J. Liu, Z. Shi and Y. Shao, An investigation of a detection method for a subsurface crack in the outer race of a cylindrical roller bearing, *Eksploracja I Niezawodnosc – Maintenance and Reliability*, vol.19, no.2, pp.211-219, 2017.
- [19] S. Khoje and S. Bodhe, Performance comparison of Fourier transform and its derivatives as shape descriptors for mango grading, *International Journal of Computer Applications*, vol.53, no.3, pp.17-22, 2012.
- [20] A. Burla, T. Haist, W. Lyda and W. Osten, Fourier descriptors for defect indication in a multiscale and multisensor measurement system, *Optical Engineering*, vol.50, no.4, 2011.
- [21] Y. Zheng, B. Guo, Z. Chen and C. Li, A Fourier descriptor of 2D shapes based on multiscale centroid contour distances used in object recognition in remote sensing images, *Sensors*, vol.19, 2019.
- [22] D. Zhang and G. Lu, Review of shape representation and description techniques, *Pattern Recognition*, vol.37, pp.1-19, 2004.
- [23] C. Direkoglu and M. S. Nixon, Shape classification via image-based multiscale descriptions, *Pattern Recognition*, vol.44, pp.2134-2146, 2011.
- [24] S. G. Mallat, A theory for multiresolution signal decomposition the wavelet representation, *IEEE Trans. Pattern Analysis and Machine Intelligence*, vol.11, no.7, pp.674-693, 1989.
- [25] S. G. Mallat, Multifrequency channel decompositions of image and wavelet models, *IEEE Trans. Acoustics Speech and Signal Processing*, vol.37, no.12, pp.2091-2109, 1989.
- [26] A. A. Nabout, Object shape recognition using wavelet descriptors, *Journal of Engineering*, vol.2013, 2013.
- [27] A. Djebala, N. Ouelaa and N. Hamzaoui, Detection of rolling bearing defects using discrete wavelet analysis, *Meccanica*, vol.43, pp.339-348, 2008.
- [28] A. Djebala, N. Ouelaa, C. Benchaabane and D. F. Laefer, Application of the wavelet multi-resolution analysis and Hilbert transform for the prediction of gear tooth defects, *Meccanica*, vol.47, pp.1601-1612, 2012.
- [29] N. Talbi, A. Metatla, N. Ouelaa, R. Younes, L. Fatmi and A. Djebala, Application of the combination of both wavelet multi-resolution analysis and empirical mode analysis to detect induction motor defects, *ICIC Express Letters, Part B: Applications*, vol.10, no.11, pp.1021-1030, 2019.
- [30] S. Osowski and D. D. Nghia, Fourier and wavelet descriptors for shape recognition using neural networks – A comparative study, *Pattern Recognition*, vol.35, pp.1949-1957, 2002.
- [31] D. C. Montgomery, *Statistical Quality Control – A Modern Introduction*, 7th Edition, John Wiley & Sons, New York, NY, USA, 2013.
- [32] J. M. Lucas and M. S. Saccucci, Exponentially weighted moving average control schemes: Properties and enhancements, *Technometrics*, vol.32, no.1, pp.1-12, 1990.
- [33] F. J. Yu, Y. Y. Yang, M. J. Wang and Z. Wu, Using EWMA control schemes for monitoring wafer quality in negative, *Microelectronics Reliability*, vol.51, pp.400-405, 2011.
- [34] N. Otsu, A threshold selection method from gray level histogram, *IEEE Trans. Systems, Man and Cybernetics*, vol.9, pp.62-66, 1979.
- [35] G. G. Amiri and A. Asadi, Comparison of different methods of wavelet and wavelet packet transform in processing ground motion records, *International Journal of Civil Engineering*, vol.7, no.4, pp.248-257, 2009.
- [36] J. S. Walker, *A Primer on Wavelets and Their Scientific Applications*, Chapman & Hall/CRC Press LLC, USA, 1999.
- [37] V. C. Vargas and L. F. D. Lopes, Comparative study of the performance of the CuSum and EWMA control charts, *Computers & Industrial Engineering*, vol.46, no.4, pp.707-724, 2004.
- [38] D. C. Montgomery and G. C. Runger, *Applied Statistics and Probability for Engineers*, 4th Edition, John Wiley & Sons, NJ, USA, 2007.
- [39] M. B. C. Khoo and S. Y. Teh, A study on the effects of trends due to inertia on EWMA and CUSUM charts, *Journal of Quality Measurement and Analysis*, vol.5, no.2, pp.73-80, 2009.
- [40] M. R. Reynolds Jr. and Z. G. Stoumbos, Comparisons of some exponentially weighted moving average control charts for monitoring the process mean and variance, *Technometrics*, vol.48, no.4, pp.550-567, 2006.